

# PCCP

Accepted Manuscript



This is an *Accepted Manuscript*, which has been through the Royal Society of Chemistry peer review process and has been accepted for publication.

*Accepted Manuscripts* are published online shortly after acceptance, before technical editing, formatting and proof reading. Using this free service, authors can make their results available to the community, in citable form, before we publish the edited article. We will replace this *Accepted Manuscript* with the edited and formatted *Advance Article* as soon as it is available.

You can find more information about *Accepted Manuscripts* in the [Information for Authors](#).

Please note that technical editing may introduce minor changes to the text and/or graphics, which may alter content. The journal's standard [Terms & Conditions](#) and the [Ethical guidelines](#) still apply. In no event shall the Royal Society of Chemistry be held responsible for any errors or omissions in this *Accepted Manuscript* or any consequences arising from the use of any information it contains.

# Fully Solution Processed All Inorganic Nanocrystal Solar Cells

Cite this: DOI: 10.1039/x0xx00000x

Troy K. Townsend,<sup>a\*</sup> and Edward E. Foos<sup>a†</sup>

Received 00th January 2012,  
Accepted 00th January 2012

DOI: 10.1039/x0xx00000x

www.rsc.org/

The effects of solution (sol) processed contacts of indium tin oxide (ITO-sol) and gold (Au-sol) on solar cells are tested. When combined with solution processed active layers of CdTe/CdSe, all-inorganic fully solution processed solar cells are produced on non-conductive glass substrates. Under AM 1.5G illumination, open circuit voltages ( $V_{oc}$ ), short circuit currents ( $J_{sc}$ ) and efficiencies ( $\eta$ ) of solar cells processed with evaporated Au and commercial ITO were found to be ( $V_{oc}=0.56\pm 0.04$  V,  $J_{sc}=17.2\pm 2.2$  mAcm<sup>-2</sup>,  $\eta=3.8\pm 0.4\%$ ), with Au-sol replacement ( $V_{oc}=0.54\pm 0.03$  V,  $J_{sc}=12.6\pm 1.0$  mAcm<sup>-2</sup>,  $\eta=2.0\pm 0.1\%$ ), with ITO-sol ( $V_{oc}=0.38\pm 0.04$  V,  $J_{sc}=12.3\pm 0.8$  mAcm<sup>-2</sup>,  $\eta=1.3\pm 0.2\%$ ), and with each layer solution processed ( $V_{oc}=0.49\pm 0.01$  V,  $J_{sc}=10.0\pm 1.5$  mAcm<sup>-2</sup>,  $\eta=1.5\pm 0.2\%$ ) with the champion fully-solution processed all-inorganic device showing  $\eta=1.7\%$ . Layers and devices were characterized with UV/Vis spectroscopy, optical profilometry, XRD, XPS and SEM. The results indicate that the reduced performance of the all-solution devices results primarily from increased roughness of the Au film and decreased conductivity of the ITO layer.

## Introduction

Given the rising global demand for power and increasing greenhouse gas emissions, the development of an economically viable solar energy system may be one of the most important challenges of the century.<sup>1</sup> Thin film inorganic solar technologies may offer an answer to this problem when paired with materials that contain high solar conversion efficiencies while exhibiting thermal, air and photostability. In addition, solution processing offers a vital cost reduction due to the added potential advantage of high throughput roll to roll printing on large and flexible surfaces.<sup>2-4</sup> Satisfying all these requirements has been the focus of recent developments for third generation solution processed solar cells with the goal of competing with existing silicon technologies.

Solution processing of organic bulk heterojunctions and inorganic semiconductor active layers has led to PV devices reaching high efficiencies ( $\eta$ ) for inorganic materials using Cu<sub>2</sub>ZnSn(Se,S)<sub>4</sub> ( $\eta=10.1\%$ )<sup>5</sup>, Cu(In,Ga)(S,Se)<sub>2</sub> ( $\eta=15.2\%$ )<sup>6</sup>, CdTe|Al single junction Schottky ( $\eta=5.15\%$ )<sup>7, 8</sup>, CdSe|CdTe heterojunction ( $\eta=3.02\%$ )<sup>9</sup>, CdTe|ZnO ( $\eta=7.1\%$ ,  $12\%$ )<sup>10, 11</sup>, TiO<sub>2</sub>|CuInS<sub>2</sub> ( $\eta=5\%$ )<sup>12</sup> and organic active layers with variations of PEDOT:PSS and P3HT:PCBM as the most common components and reaching 10% efficiency and higher.<sup>13</sup> While some of these examples employ a single solution processed contact (i.e. AgNWs<sup>14</sup>, Ag nanocrystal paint,<sup>15</sup> graphite<sup>12</sup>), each still uses vacuum sputtered transparent conductive oxides (TCOs),<sup>5-10, 12, 14-17</sup> e-beam evaporated metal contacts<sup>5-10, 16, 17</sup> or metal contact substrates where the device was built on patterned copper<sup>18</sup> as the second electrode. Recently, however, a fully solution processed device built on plastic was reported

using organic active layers and conductive back contact to reach 2.0% efficiency.<sup>19</sup>

While progress on organic photovoltaics is rapidly growing, inorganic devices still hold the record for highest efficiencies which is in part due to their broad spectral absorption and excellent electronic properties (i.e. recently First Solar Inc. has achieved 20.4% efficiency for thin film CdTe solar cells). Considering the recorded higher efficiencies and lower cost per watt<sup>4</sup> compared to organic devices,<sup>17</sup> combined with the enhanced thermal and photo-stability of bulk-scale inorganic materials, we focused on an all-inorganic based structure for fabrication of a top to bottom all solution-based solar cell. Unfortunately, a major disadvantage compared to organics is that inorganic materials are difficult to deposit from solution. One way to overcome this problem while retaining the attractive qualities of inorganics is to synthesize the materials on the nanoscale. Inorganic nanocrystals encased in an organic ligand shell are soluble in organic solvents and can be deposited from solution (spin-, dip-, spray-coat). After ligand removal and sintering (excluding non-sintered semiconductor nanocrystals like PbS and PbSe which also benefit from size-controlled quantum confinement effects),<sup>20, 21</sup> these nanocrystals form more continuous films with improved properties. Fortunately, the high surface areas of nanostructures promote lower melting/sintering temperatures than are required for bulk-scale inorganics, opening more options for temperature sensitive substrates (i.e. plastics, fabrics etc.).<sup>22, 23</sup> Examples of solution processing inorganic nanocrystals include the use of metallic<sup>24</sup> and semiconducting inks<sup>4, 25, 26</sup> or metal precursor complexes.<sup>6</sup> As a result of this research, solar devices have been fabricated from nanoscale CdTe/CdSe particle inks on

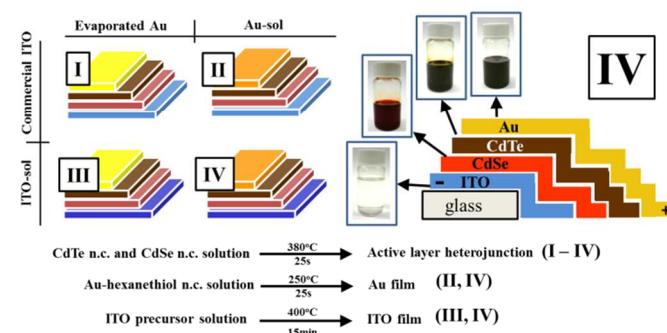
pre-made TCOs with e-beam or thermally evaporated low work function metal contacts.<sup>7, 25, 27</sup>

In an attempt to step away from conventional evaporated contacts and explore the use of solution processed transparent conductive electrodes, materials like graphene, carbon nanotubes, silver nanowires and combustion processed ITO were considered based on their figure of merit (FOM = electrical conductivity divided by optical conductivity).<sup>28</sup> While the use of Ag nanowires as transparent conductive contacts has shown promise recently, especially considering their mechanical flexibility, this material shows temperature sensitivity and is not as robust against oxidation as conventional TCOs.<sup>29</sup> Fortunately, solution-based combustion synthesis of indium tin oxide (ITO), zinc tin oxide (ZTO), indium zinc oxide (IZO) among other transparent conductive oxide films displayed comparable transparency (>80%) and conductivity ( $680 \text{ Scm}^{-1}$ ) to conventional TCOs made by sputter deposition.<sup>30</sup> This solution process involves the use of metal salt precursors dissolved in an oxidizing solution, which upon exposure to heat (250–450°C) produces an exothermic reaction with elevated local temperatures to produce high quality films of ITO. To complement this solution-based TCO, we have utilized thiol-derivatised gold metal nanoparticle<sup>31</sup> solutions that produce metallic films after spray deposition<sup>32</sup> and a low temperature annealing (150–250°C).<sup>33</sup> Given the high work functions of ITO and Au contacts, the need for a heterojunction structure to separate charge at the semiconductor-semiconductor interface became apparent. Lower work function metals would be ideal for forming ohmic contacts with the n-type layer; however, most of these metals (Ca, Li, Al) are susceptible to spontaneous oxidation, especially at the nanoscale. Considering the ease of the one-step synthesis of CdSe and CdTe, we chose this heterojunction structure to use as a proof of concept active layer for a truly complete solution processed inorganic solar cell. For this study, solution-based ITO was spin coated onto a glass microscope slide followed by CdSe, CdTe and Au nanocrystals. Each of these materials was deposited in a layer-by-layer iterative process with thermal annealing to convert nanoscale precursors into more bulk-like films while simultaneously removing organic ligands to improve charge transport.

## Results and Discussion

Solution processed photovoltaic devices were constructed following an inverted architecture as depicted in Scheme 1.<sup>34</sup> In order to systematically evaluate the effect of solution-based electrodes, four separate samples were examined. Devices [I–IV] each contain conventional solution-processed CdSe and CdTe photo-active layers prepared from nanocrystal (3–5 nm) stock solutions. Device [I] was constructed with pristine commercial ITO and evaporated Au contacts, and this structure is analogous to other reports on “solution-processed” photovoltaics where the front and back electrode are deposited using evaporation or sputtering based techniques. Device [II] is modified from [I] where the Au metal was deposited via thiol-capped Au nanocrystals (2–5 nm) dispersed in chloroform. Likewise, device [III] is modified from [I] where the transparent conductive electrode (commercial ITO) was replaced with solution processed ITO (ITO-sol) from a metal ion precursor solution containing indium and tin salts.<sup>30</sup> Finally, the all-solution devices were prepared entirely from solution on glass substrates with the structure ITO-sol/CdSe-sol/CdTe-sol/Au-sol [Device IV]. These solution processed films were

then characterized with SEM and optical profilometry to assess surface morphologies, surface roughness, and film thicknesses.



**Scheme 1.** Deposition scheme of four device architectures starting with solution processing of only the nanocrystal (n.c.) active layers with the typical pristine evaporated ITO and Au contacts [I], with Au-sol contact [II], with ITO-sol contact [III], and the all-solution device [IV] including photos of each precursor solution.

After annealing, the morphologies of each layer surface were imaged with SEM and shown in Figure 1. Commercial ITO contains characteristic large (>100 nm) crystallite grains of the high purity material (Figure 1A); whereas ITO-sol contains smaller nanoscale grains ( $15.7 \pm 2 \text{ nm}$ ) as a result of the combustion process (Figure 1B). Smaller ITO grain sizes have been previously correlated to higher sheet resistances in response to processing parameters such as oxygen partial pressure and increased purity.<sup>35, 36</sup>

The evaporated Au contact (140 nm thick) displays large grains (100–300 nm, Figure 1C) with low Root Mean Square (RMS) roughness ( $5.1 \pm 2.6 \text{ nm}$ ) while Au-sol contains smaller crystallites (50–100 nm, Figure 1D). However, because the metallic back contact is highly conductive, grain size plays a smaller role compared to semiconductor TCOs. The Au-sol precursor solution could not be spin-coated due to its low viscosity which would cause it to leak out under the mask and blend with the other contacts. Instead, Au nanocrystals were spray-cast with a gravity-fed airbrush<sup>32</sup> which facilitated rapid solvent drying leaving behind discrete contacts without blending. This modified deposition process resulted in 12 times higher surface roughness ( $61 \pm 3.5 \text{ nm}$ ) due to the rapid drying and non-uniformity of the spray deposition process.<sup>37, 38</sup>

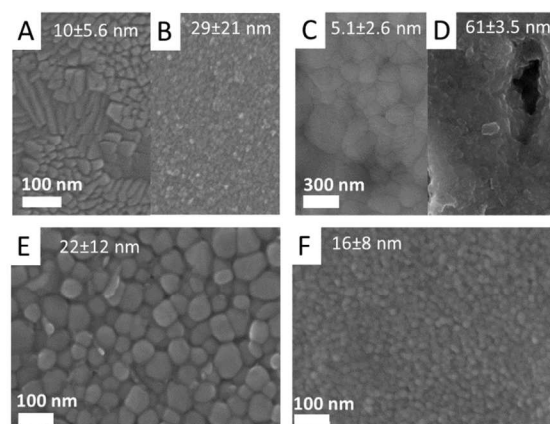


**Figure 1.** SEM images with RMS roughness values (nm) of commercial ITO [A] and ITO-sol [B] bottom electrode films on glass, evaporated gold [C] and Au-sol [D] top contacts, with CdTe-sol [E] and CdSe-sol [F] active layer films.

The CdTe and CdSe nanocrystals (3-5 nm) were spin-coated on ITO and annealed at 380°C in the presence of CdCl<sub>2</sub>(s) to promote grain growth to 50-80 nm for CdTe (Figure 1E) and 10-15 nm for CdSe (Figure 1F). These active layers were found to be relatively smooth (16–22 nm RMS roughness).

Based on the SEM images, each of these solution processed materials show crystal grains of various size ranges based on the route of fabrication. In order to verify the crystallinity and phase of each of these layers, XRD patterns were taken and shown together with the completed all-solution device [IV] and device [I] with pristine contacts (Figure 2A-F). Each XRD pattern matches those previously reported for these materials and the completed devices contain reflection peaks originating from each separate layer. Notably, the peaks corresponding to ITO at  $2\theta=30.56^\circ$  and  $2\theta=35.44^\circ$  show a higher intensity for the cell built on ITO-sol (Figure 2E, F). This comes as a result of the reduced thickness of the commercial ITO (120 nm) vs. the ITO-sol (360 nm) as measured by optical profilometry. Due to the lower conductivity of ITO-sol (315 Scm<sup>-1</sup> vs. 6940 Scm<sup>-1</sup> for commercial ITO as determined from 4-point probe measurements), ITO-sol is required to be thicker in order to reach a sheet resistance of 150-250 Ω/□ compared to 8-12 Ω/□ for commercial ITO.

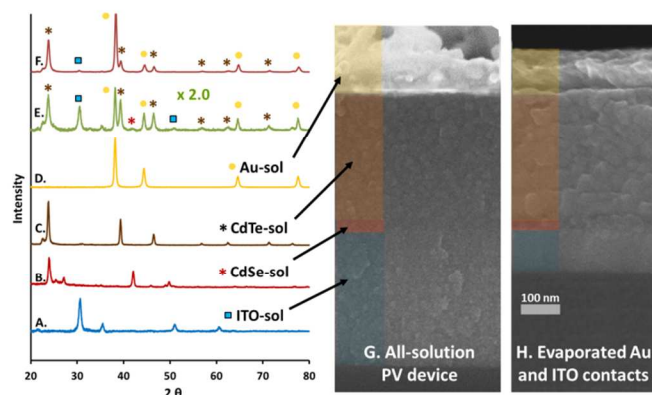


Figure 2. XRD patterns of each individual layer of ITO-sol [A], CdSe-sol [B], CdTe-sol [C], and Au-sol [D] and the completed cell (x2.0 intensity for clarity) containing each layer as ITO-sol/CdSe-sol/CdTe-sol/Au-sol [E] including a cell with evaporated contacts as ITO/CdSe-sol/CdTe-sol/Au [F] and cross-section SEM images of the all-solution device (Device IV) [G] and the device built with evaporated contacts (Device I) [H].

In order to assess the effect of the increased thickness of the ITO-sol on the transmission of light through the device, UV/Vis spectra were taken of these films after annealing. Surprisingly, optical transmission spectra of commercial ITO (120 nm) and ITO-sol (360 nm) show minimal differences in the visible range (Figure 3A) indicating sufficient light penetration to the active layers. ITO-sol shows higher absorption in the UV region between  $\lambda = 300-350$  nm as a result of increased absorption from Sn content and layer thickness. Visible light is transmitted through the ITO contact and absorbed by CdSe and CdTe.<sup>34</sup> Absorption spectra of single layer CdSe (60 nm), single layer CdTe (400 nm, thickness measured from optical profilometry) and the combined heterojunction are shown in Figure 3A. As demonstrated by Carter et al., these active layers must be thinner than commercially produced CdTe films, which are typically several micrometers in thickness, because the nanocrystalline nature of these solution processed films produce shorter diffusion lengths as a result of the reduced charge carrier lifetimes.<sup>9</sup> The optimal thickness of these films

results from an interplay between increasing light absorption and increasing recombination at grain interfaces. However, annealing the nanocrystal films in the presence of CdCl<sub>2</sub> promotes grain growth (>10 times). This is observable by SEM (Figure 1E-F) and is supported by the UV/Vis spectra where the CdSe and CdTe nanocrystal precursors display quantum confinement whereas the annealed films resemble bulk-like films. Red shifted onsets for CdSe from  $\lambda=564$  nm to 678 nm and CdTe from 635 nm to 850 nm occurs after sintering (Figure 3) indicating a transition from nanoscale crystals to bulk-like films.

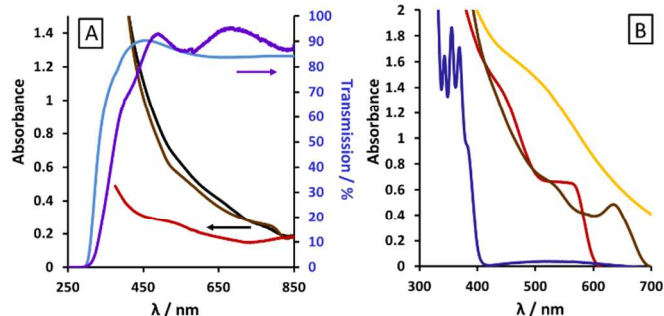


Figure 3. UV-Vis transmission of commercial ITO (light blue) and ITO-sol (purple) on glass and absorption of CdSe-sol (red), CdTe-sol (brown) and CdSe-sol/CdTe-sol films together (black) on commercial ITO glass substrates [A], and absorption of nanocrystal precursor solutions of CdSe (red), CdTe (brown), Au (gold), and ITO (purple) prior to annealing [B].

After verifying the surface morphologies, layer thicknesses, crystallinity and optical properties of each solution processed material, these films were deposited in a layer-by-layer process on non-conductive glass substrates. These fully solution processed devices were systematically compared to equivalent devices with non-solution processed contacts (four devices as described in Scheme 1). In order to evaluate the photovoltaic properties of the four structures, devices were illuminated under simulated one sun and the current-voltage curves of typical devices for each structure are shown in Figure 4.

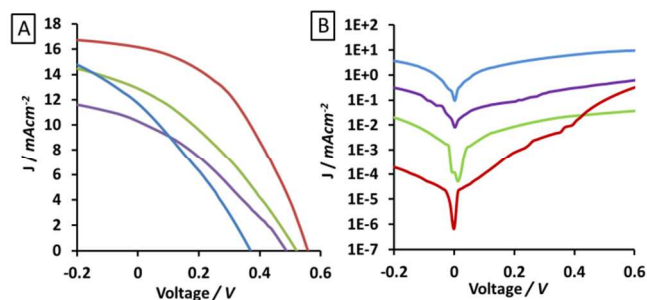


Figure 4. Measured light J-V curves for representative solar devices [I] (red), [II] (green), [III] (blue) and [IV] (purple) which are 0.1 cm<sup>2</sup> masked device squares formed from the intersection of ITO and Au contacts and illuminated through the ITO-glass side under AM 1.5G filtered spectral illumination (100 mWcm<sup>-2</sup>) [A], and the dark JV curves for the same devices [B].

Notably, the short circuit current is most affected by the change from evaporated to solution processed metal cathodes where Device I was measured as 17.2±2.2 mAcm<sup>-2</sup> followed by 12.6±1.0 mAcm<sup>-2</sup> for Device II (Table 1). This observation points to the hypothesis that the actual contact area is lower for sprayed Au nanocrystal films compared to evaporated metal.

Given that the roughness of the solution processed films is 12 times as high ( $61 \pm 3.5$  nm RMS) compared to ( $5.1 \pm 2.6$  nm for evaporated Au films), this difference would account for the apparent loss of current density over the same device area.

Similarly, solution processing of the ITO anode produced a drop in the open-circuit voltages where Device I showed  $0.56 \pm 0.04$  V whereas Device III gave  $0.38 \pm 0.04$  V. Since these electrodes are relatively smooth ( $29 \pm 21$  nm RMS for ITO-sol), this drop in voltage should instead be a result of decreased conductivity, which is also consistent with the decrease in the shunt resistivity (Rsh). Apart from the layer conductivity, the interface between ITO/CdTe may also play an important role, and this was previously found to greatly affect the Voc in solution processed solar cells.<sup>11</sup> This may provide insight into the reasons for the low Voc for Device III, which might be explained by a lack of annealing of the evaporated Au contact, whereas Devices II and IV were both heated to  $250^\circ\text{C}$  for 25s to remove thiol ligand. This unique processing history may serve to improve the junctions between the electrodes and the active layers as was found to be true in other photovoltaic systems.<sup>39</sup>

**Table 1.** Summary of performance of solution processed heterojunction solar cells (ITO/CdSe/CdTe/Au) in the dark and under AM 1.5G filtered spectral illumination ( $100 \text{ mW/cm}^2$ ) including shunt resistivity (Rsh) and series resistivity (Rs). The device area is  $0.1 \text{ cm}^2$ .

Device	Rsh ( $\Omega\text{cm}^2$ )	Rs ( $\Omega\text{cm}^2$ )	Voc (V)	Jsc ( $\text{mA/cm}^2$ )	Fill Factor (%)	Efficiency (%)
[I] ITO-commercial Au-evaporated	$1.50 \times 10^6$	8.35	$0.56 \pm 0.04$	$17.2 \pm 2.2$	$40.1 \pm 1.4$	$3.75 \pm 0.4$
[II] ITO-commercial Au-sol	$2.89 \times 10^5$	24.7	$0.54 \pm 0.03$	$12.6 \pm 1.0$	$29.1 \pm 2.5$	$1.95 \pm 0.1$
[III] ITO-sol Au-evaporated	$3.74 \times 10^2$	33.0	$0.38 \pm 0.04$	$12.3 \pm 0.8$	$28.6 \pm 1.1$	$1.34 \pm 0.2$
[IV] ITO-sol Au-sol	$5.82 \times 10^3$	21.7	$0.49 \pm 0.01$	$10.0 \pm 1.5$	$31.6 \pm 0.8$	$1.53 \pm 0.2$

Importantly, the dark current (leakage current) increases as the electrodes are replaced with solution processing (Figure 4B). This is made evident by the decreasing Rsh from  $\sim 10^6 \Omega\text{cm}^2$  for the pristine contacts to  $\sim 10^3 \Omega\text{cm}^2$  for the all-solution processed cell (Device IV) and increasing series resistivity (Rs) from  $8.3 \Omega\text{cm}^2$  to  $21.7 \Omega\text{cm}^2$  although this change is not as pronounced (Table 1). Because the shunt resistance plays a larger role in these devices, more attention should be dedicated to improving the interfaces between these solution processed layers in order to minimize leakage current.

The minimal differences between devices III and IV reveal that the impact of switching to the ITO-sol contact is greater than replacing Au-evaporated with Au-sol. This points to the observation that the intrinsic material properties have a larger impact on charge transport than surface roughness. In order to gain a better understanding of the reason for reduced efficacy in these films, Argon plasma-etched X-ray photoelectron spectroscopy (XPS) was used to determine the level of surface and sub-surface impurities of the electrodes. Figure 5 shows the C 1s, O 1s, and Au 4f peak regions for solution processed Au (A,B,C) and sub-surface C 1s, In 3d, and Sn 3d for commercial ITO and ITO-sol (D,E,F). The peak positions for each metal correspond to the presence of  $\text{Au}^0$  and oxygen-bound In (III)-O and Sn (IV)-O ions. These energies remain unchanged between commercial ITO and ITO-sol, confirming their similarities of composition. Interestingly, despite the carbon-rich nature of the thiol-capped-Au nanocrystal, after annealing at  $250^\circ\text{C}$ , there is

no evidence of residual impurities from the ligand in the film. However, surface carbonaceous species (Figure 5A, B) were detected, and this is not surprising considering both S and C have negligible solubility in solid gold and should be concentrated at the surface after heating.<sup>40</sup> Annealing at higher temperatures ( $\sim 300^\circ\text{C}$ ) in the presence of air has also shown to further volatilize S and C adsorbates from gold nanocrystal films.<sup>33</sup> The carbon peak at  $284.6 \text{ eV}$  corresponds to surface C-C bonds from adventitious carbon common to air-exposed samples. Since the contribution of surface adsorbed C and O species to the conductivity of the film is considered to be negligible, an analysis of subsurface impurities was conducted with Ar-plasma etching. Peak analysis revealed subsurface  $\text{Au}^0$  without oxygen, carbon, or sulfur (Figure 5B inset) impurities, verifying the quality of this material and further supporting that the higher surface roughness is the major reason for lower photo-current densities. The ITO-sol, however, showed 6.29% subsurface carbon content as a product of the combustion process (Figure 5D), and this is in contrast to commercial ITO which did not show detectable carbon content in the film. The carbon peak at  $285.1 \text{ eV}$  corresponds to aliphatic carbons indicating incomplete combustion of the organic solvent. This could be avoided with carbon-free solvents which we are currently investigating in our laboratory.

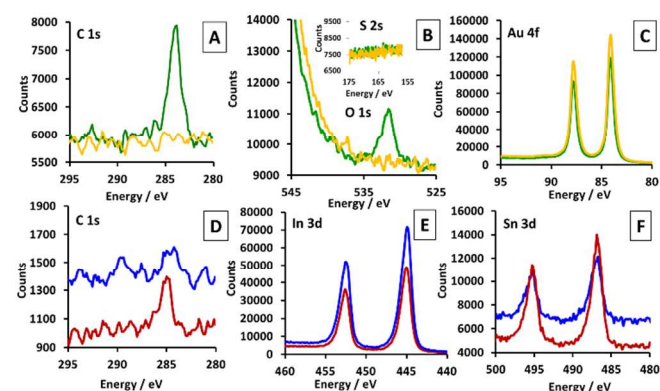


Figure 5. X-ray photoelectron spectra (XPS) of solution processed Au cathodes detecting the surface (green) and sub-surface (yellow) presence of carbon [A], oxygen [B], sulphur [B inset] and gold (O) [C] and the content of carbon [D], indium (III) [E] and tin (IV) [F] of sub-surface commercial ITO (blue) and solution processed ITO (red).

Because ITO-sol is relatively smooth ( $29 \pm 21$  nm RMS), the decrease in conductivity compared to commercial ITO is most likely the reason for the lower current densities of Devices III and IV. This comes as a combined result of smaller crystallite grains and carbon impurities. However, since impurities are not an issue for Au-sol as revealed by XPS, the loss in photocurrent is largely attributed to the high surface roughness (porosity) of the electrode which limits contact with the CdTe absorbing layer. Improving film qualities and interfaces via lower surface roughness, improved layer contact wetting, reducing impurity content and improving the crystallinity of these solution processed layers should result in enhanced device performance.

## Conclusions

In a step-by-step method, complete inorganic photovoltaic devices were constructed on non-conductive glass substrates at moderate temperatures using a solution process for each layer.

This was made possible for inorganic materials (which are not conventionally solution processable) via the implementation of soluble inorganic nanocrystals encased in an organic ligand shell. All device layers were solution processed including the back contact (thiol-capped Au nanocrystals), the transparent conductive ITO film (In (III) and Sn (IV) salts stabilized with 2-methoxyethanol and an oxidizer) and the photo-active layers (pyridine-capped CdSe and CdTe nanocrystals). After sintering, ligand removal promoted enhanced film qualities of each material and device efficiencies reached  $\eta = 1.7\%$  for ITO-sol/ CdSe-sol/ CdTe-sol/ Au-sol. Further studies are needed to weigh the inherent cost reduction of fabrication and installation for completely solution based photovoltaics (drop-, spin-, spray-coating) with the present lower efficiencies. Improving the quality of these solution processed films and their interface with the active layers through careful control over unique processing steps will be the next challenge for these emerging technologies. Specifically, steps should be taken toward reducing the surface roughness of the electrode films enabling higher interlayer contact and reducing impurities through chemical treatments which would simultaneously improve grain size and charge transport. The electrode ink processing used in this study is also applicable to other high performance ( $>10\%$   $\eta$ ) solution processable inorganic active layers such as CdTe/ZnO,  $\text{Cu}_2\text{ZnSn}(\text{Se},\text{S})_4$ , or  $\text{Cu}(\text{In},\text{Ga})(\text{S},\text{Se})_2$ , which could lead to devices with further enhanced performance. In addition, the transition to less expensive conductive electrodes such as aluminium and carbon would minimize materials costs while maintaining the intrinsic freedoms of solution deposition onto large and irregular surfaces.

## Materials and Methods

### ITO Precursor Solution Preparation

Adapted and optimized from a procedure by Marks et al. 2011,<sup>30</sup> solid salts of  $\text{In}(\text{NO}_3)_3 \cdot 2.85\text{H}_2\text{O}$  (2.93g, 0.832 M) and  $\text{SnCl}_2 \cdot 2\text{H}_2\text{O}$  (0.357g, 0.158 M) were dissolved in a 10 mL 2-methoxyethanol solution containing  $\text{NH}_4\text{OH}$  as a pH stabilizer (167  $\mu\text{L}$ , 0.242 M) and  $\text{NH}_4\text{NO}_3$  as an oxidizer (0.83g, 1.04 M). This hazy white solution was sonicated for 20 min until it became colorless and transparent.

### Au Nanocrystal Synthesis

Au nanocrystals were synthesized in air at room temperature following Brust et al. 1994<sup>31</sup> where (1.518g, 3.85 mmol) of  $\text{HAuCl}_4 \cdot 3\text{H}_2\text{O}$  was dissolved into 126 mL  $\text{H}_2\text{O}$  to produce a yellow solution. A mixture of (9.52 g, 17.4 mmol) tetraoctylammonium bromide dissolved in 334 mL toluene was added and stirred vigorously until all the tetrachloroaurate was transferred to the organic layer. The ligand, (0.452g, 3.82 mmol hexanethiol in 2 mL toluene) was added to the top toluene phase of the bilayer. A freshly prepared aqueous mixture of (1.58g, 41.8 mmol)  $\text{NaBH}_4$  in 105 mL  $\text{H}_2\text{O}$  was slowly added dropwise with continued stirring. After a further 3 h of stirring, the organic phase was separated and evaporated to 20 mL with

a rotary evaporator. The product was re-dispersed with 50 mL hexanes and washed with 200 mL of methanol four times with centrifugation to remove excess ligand then dried under ambient conditions. Yield after annealing to remove ligand was 0.54 g (71%).

### Active Layer Nanocrystal Synthesis

CdTe and CdSe nanocrystals were synthesized following a literature procedure.<sup>27, 41</sup> Briefly, 0.48 g CdO, 4.29 g oleic acid and 76 mL of 1-octadecene were combined in a 250 mL 3-neck flask. This solution was evacuated at 100°C for 20 min then filled with Ar and brought to 260°C. Tellurium (0.24 g) or Selenium (0.153 g) powder was sonicated in 4.39 g trioctylphosphine (TOP), combined with 5 g 1-octadecene and injected into the flask after removing from heat at 260°C for CdTe or 250°C for CdSe nanocrystals. The reaction was cooled naturally to room temperature and the resulting nanocrystals were precipitated with the addition of 75 mL heptane and 150 mL ethanol. They were re-dissolved in 5 mL pyridine and heated under Ar for 18 h at 85°C. Following this pyridine exchange, the nanocrystals were precipitated in 40 mL hexanes to remove excess ligands and re-dissolved in a 5 mL pyridine / 5 mL 1-propanol mixture to produce 40 mg/mL CdTe and 16 mg/mL CdSe nanocrystal stock solutions.

### Device Fabrication

Devices I and II were built on commercially available indium-tin oxide (ITO, 8-12  $\Omega/\square$  Delta Technologies) coated glass substrate (25 mm by 25 mm by 1.1 mm) and devices III and IV were built on glass microscope slides (25 mm by 25 mm by 1.0 mm) which were first sonicated in acetone and ethanol and blown dry using  $\text{N}_2$ . Solution processed ITO (ITO-sol) was formed by spin coating a thin film of the precursor solution onto the glass substrate at 4500 rpm for 20 s in air and quickly placing on a hotplate set to 400°C to sinter for 15 min. This cycle was repeated (6-7 times) until the desired film thickness (200-500 nm), transparency (85 %  $> \lambda = 400$  nm) and sheet resistance ( $R < 250 \Omega$ ) was obtained. Using scotch tape to mask strips of ITO, both commercial ITO and ITO-sol substrates were etched in a 10% aqueous aqua regia solution set at 60°C until the glass was exposed to produce patterned ITO of 0.318 cm strips to allow for the construction of multiple devices on each substrate. These substrates were then cleaned with ethanol followed by brief 3s dipping in 10% by volume aqua regia at room temperature and rinsing with water. Drops of silver epoxy were painted onto the ITO electrodes and annealed at 380°C to insure direct contact with the ITO anode prior to device fabrication. This was found to be necessary due to the difficulty of scratching the active layers to expose the ITO for ohmic contact after CdSe/CdTe annealing.

The active layers were then deposited starting with CdSe (16 mg/mL) and followed by CdTe (40 mg/mL). These nanocrystal stock solutions were spin coated at 850 rpm for 30s onto the ITO substrate and dried at 150°C for 1 min to remove solvent. After cooling to room temperature, the nanocrystal film was dipped in a 25°C saturated  $\text{CdCl}_2/\text{MeOH}$  solution heated to

60°C, then immediately dipped into iPrOH to remove excess CdCl<sub>2</sub> and blown dry with N<sub>2</sub>. The film of nanocrystals (3-5 nm) was placed on a hot plate at 380°C for 25s to induce sintering and form larger grains (50-100 nm). After cooling to room temperature, the film was rinsed in water to remove excess CdCl<sub>2</sub>. This process was repeated iteratively to build the CdSe and CdTe films layer-by-layer to reach the desired thicknesses of each material, typically 3 layers for 60 nm thick CdSe and 6 layers for 400 nm thick CdTe.<sup>27, 42-43</sup> Devices I and III were completed with thermally evaporated gold contacts with an Edwards Auto 306. The samples were pumped under vacuum to ~10<sup>-7</sup> Torr and using a shadow mask, 140 nm Au was deposited onto the CdTe surface. Devices II and 4 were completed in air using the gold nanocrystal solutions. Samples were masked with tape and 2 mL of the Au nanocrystal solution dispersed in chloroform (70 mg/mL) was sprayed from a gravity-fed Paasche VSR90#1 airbrush equipped with a 0.5 mm needle and one velocity setting until all of the solution was transferred (~30s duration) and a dark black film formed. The nanocrystals were applied uniformly using a rapid side-to-side passing spray perpendicular to the substrate at a distance of 60 mm from the spray nozzle. The spray pressure of N<sub>2</sub> carrier gas was controlled with a regulator set to 20 psi. The entire cell was then heated at 250°C for 20 sec on a hotplate to anneal the Au nanocrystals and remove thiol ligands to form a gold film. Each type of gold contact was masked to form 0.318 cm wide strips orthogonal to the patterned ITO to ultimately produce 10 square devices per 6.25 cm<sup>2</sup> substrate each with an area of 0.10 cm<sup>2</sup>.

### Characterization and Device Testing

Film morphology, thickness and surface roughness were determined with a Leo 1550 SEM and a Zygo optical profilometer. X-ray diffraction patterns were taken with a Smart Lab Rigaku X-ray Diffractometer under two degree grazing incidence mode. X-ray photoelectron spectra were taken with a Thermo Scientific K-alpha XPS equipped with Ar sputter depth profiling. The current density-voltage characteristics of the photovoltaic devices were measured with an Oriel PVIV-1A Test Station where solar cell efficiency was measured under the spectral output from a 150 W solar simulator (Newport) using an air mass 1.5 global (AM 1.5G) filter. The irradiance (100 mW/cm<sup>2</sup>) of the solar simulator was adjusted using a reference cell 91150V (Newport) traceable to the National Renewable Energy Laboratory (NREL). Shunt resistivities were calculated from the slope of the dark current IV curves and series resistivities were determined from the multi-light method.<sup>44</sup> Sheet resistances and resistivities of the contacts were calculated from a four point probe measurement.

### Acknowledgements

The Office of Naval Research (ONR) is gratefully acknowledged for financial support. Special thank you to Dr. Woojun Yoon for photovoltaic testing of preliminary devices and to Dr. Carl Giller for advice. This work was conducted while T. Townsend held a National Research Council Postdoctoral Fellowship at the Naval Research Laboratory.

### Notes and references

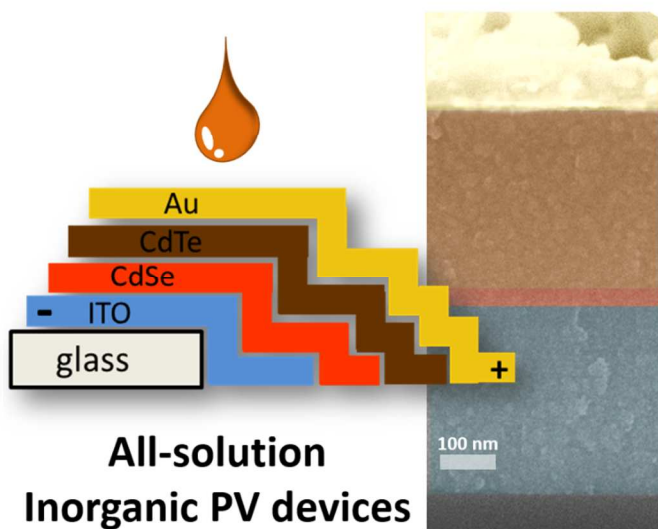
<sup>a</sup> Naval Research Laboratory, Washington, DC 20375

\*Current affiliation is St. Mary's College of Maryland

†Current affiliation is Indian Head Naval Surface Warfare Center

- 1 V. Fthenakis, J. E. Mason, and K. Zweibel, *Energy Policy*, 2009, **37**, 387–399.
- 2 K. Zweibel, *Sol. Energy Mater. Sol. Cells*, 1999, **59**, 1–18.
- 3 C. J. Brabec, *Sol. Energy Mater. Sol. Cells*, 2004, **83**, 273–292.
- 4 S. E. Habas, H. A. S. Platt, M. F. A. M. van Hest, and D. S. Ginley, *Chem. Rev.*, 2010, **110**, 6571–6594.
- 5 D. A. R. Barkhouse, O. Gunawan, T. Gokmen, T. K. Todorov, and D. B. Mitzi, *Prog. Photovolt. Res. Appl.* 2012, **20**, 6–11.
- 6 T. K. Todorov, O. Gunawan, T. Gokmen, and D. B. Mitzi, *Prog. Photovolt. Res. Appl.*, 2013, **21**, 82–87.
- 7 J. D. Olson, Y. W. Rodriguez, L. D. Yang, G. B. Alers, and S. A. Carter, *Appl. Phys. Lett.* 2010, **96**, 242103–242103-3.
- 8 S. Sun, H. Liu, Y. Gao, and D. Qin, and J. Chen, *J. Mater. Chem.* 2012, **22**, 19207–19212.
- 9 T. Ju, L. Yang, and S. A. Carter, *J. Appl. Phys.* 2010, **107**, 104311–1–104311-5.
- 10 B. I. MacDonald, A. Martucci, S. Rubanov, S. E. Watkins, P. Mulvaney, and J. J. Jasieniak, *ACS Nano* 2012, **6**, 5995–6004.
- 11 M. G. Panthani, J. M. Kurley, R. W. Crisp, T. C. Dietz, T. Ezzyat, J. M. Luther, and D. V. Talapin, *Nano Lett.* 2013, **14**, 670–675.
- 12 M. Nanu, J. Schoonman, and A. Goossens, *Nano Lett.* 2005, **5**, 1716–1719.
- 13 T. Ameri, P. Khoram, J. Min, and C. J. Brabec, *Adv. Mater.* 2013, **25**, 4245–4266.
- 14 C. C. Chen, L. Dou, R. Zhu, C. H. Chung, T. B. Song, Y. B. Zheng, S. Hawks, G. Li, P. S. Weiss, and Y. Yang, *ACS Nano* 2012, **6**, 7185–7190.
- 15 B. Park, Y. Chan Kim, and S. H. Yun, *J. Mater. Chem. A* 2013, **1**, 2030–2038.
- 16 L. Ming-Yi, L. Chun-Yu, S. Shu-Chia, S. Jen-Yu, L. Yu-Hong, W. Wen-Hau, and L. Ching-Fuh, IEEE Photovoltaic Spec. Conf., 35th, 2010.
- 17 V. C. Tung, J. H. Huang, J. Kim, A. J. Smith, C. W. Chu, and J. Huang, *Energy Environ. Sci.* 2012, **5**, 7810–7818.
- 18 T. S. Kim, S. I. Na, S. H. Oh, R. Kang, B. K. Yu, J. S. Yeo, J. Lee, and D. Y. Kim, *Sol. Energy Mater. Sol. Cells* 2012, **98**, 168–171.
- 19 J. H. Yim, S. Y. Joe, C. Pang, K. M. Lee, H. Jeong, J. Y. Park, Y. H. Ahn, J. C. de Mello, and S. Lee, *ACS Nano* 2014, **8**, 2857–2863.
- 20 J. J. Choi, Y. F. Lim, M. E. B. Santiago-Berrios, M. Oh, B. R. Hyun, L. Sun, A. C. Bartnik, A. Goedhart, G. G. Malliaras, H. C. D. Abruña, F. W. Wise, and T. Hanrath, *Nano Lett.* 2009, **9**, 3749–3755.
- 21 W. Yoon, J. E. Boercker, M. P. Lumb, D. Placencia, E. E. Foos, J. G. Tischler, *Sci. Rep.* 2013, **3**, 1–7.
- 22 A. N. Goldstein, C. M. Echer, and A. P. Alivisatos, *Science* 1992, **256**, 1425–1427.
- 23 P. Buffat, and J. P. Borel, *Phys. Rev. A* 1976, **13**, 2287–2298.

- 24 G. Norsworthy, C. R. Leidholm, A. Halani, V. K. Kapur, R. Roe, B. M. Basol, and R. Matson, *Sol. Energy Mater. Sol. Cells* 2000, **60**, 127–134.
- 25 I. Gur, N. A. Fromer, M. L. Geier, and A. P. Alivisatos, *Science* 2005, **310**, 462–465.
- 26 I. E. Anderson, A. J. Breeze, J. D. Olson, L. Yang, Y. Sahoo, and S. A. Carter, *Appl. Phys. Lett.* 2009, **94**, 063101–063101-3.
- 27 J. Jasieniak, B. I. MacDonald, S. E. Watkins, and P. Mulvaney, *Nano Lett.* 2011, **11**, 2856–2864.
- 28 D. S. Hecht, L. B. Hu, and G. Irvin, *Adv. Mater.* 2011, **23**, 1482–1513.
- 29 J. L. Elechiguerra, L. Larios-Lopez, C. Liu, D. Garcia-Gutierrez, A. Camacho-Bragado, and M. J. Yacaman, *Chem. Mater.* 2005, **17**, 6042–6052.
- 30 M. G. Kim, M. G. Kanatzidis, A. Facchetti, and T. J. Marks, *Nat. Mater.* 2011, **10**, 382–388.
- 31 M. Brust, M. Walker, D. Bethell, D. J. Schiffrin, and R. Whyman, *J. Chem. Soc., Chem. Commun.* 1994, **0**, 801–802.
- 32 H. Wohltjen, A. W. Snow, *Anal. Chem.* 1998, **70**, 2856–2859.
- 33 M. B. Cortie, M. J. Coutts, C. Ton-That, A. Dowd, V. J. Keast, and A. M. McDonagh, *J. Phys. Chem. C* 2013, **117**, 11377–11384.
- 34 W. Yoon, T. K. Townsend, M. P. Lumb, J. G. Tischler, E. E. Foos, *IEEE Trans. Nanotechnol.* 2014, **PP**, 1–7.
- 35 A. K. Kulkarni, K. H. Schulz, T. S. Lim and M. Khan, *Thin Solid Films*, 1999, **345**, 273–277.
- 36 N.-R. Kim, J.-H. Lee, Y.-Y. Lee, D.-H. Nam, H.-W. Yeon, S.-Y. Lee, T.-Y. Yang, Y.-J. Lee, A. Chu, K. T. Nam and Y.-C. Joo, *J. Mater. Chem. C*, 2013, **1**, 5953–5959.
- 37 E. E. Foos, W. Yoon, M. P., J. G. Tischler and T. K. Townsend, *ACS Appl. Mater. Inter.*, 2013, **5**, 8828–8832.
- 38 T. K. Townsend, W. Yoon, E. E. Foos and J. G. Tischler, *ACS Appl. Mater. Inter.*, 2014, **6**, 7902–7909.
- 39 S. C. Gong, S. K. Jang, S. O. Ryu, H. Jeon, H. H. Park, H. J. Chang, *Curr. Appl. Phys.* 2010, **10**, 192–196.
- 40 B. J. Tan, P. M. A. Sherwood and K. J. Klabunde, *Langmuir*, 1990, **6**, 105–113.
- 41 W. W. Yu, and X. Peng, *Angew. Chem. Int. Ed.* 2002, **41**, 2368–2371.
- 42 A. Javier, and E. E. Foos, *IEEE Trans. Nanotechnol.* 2009, **8**, 569–573.
- 43 W. Yoon, E. E. Foos, M. P. Lumb, and J. G. Tischler, IEEE Photovoltaic Spec. Conf., 38th, 2012.
- 44 K. C. Fong, K. R. McIntosh, and A. W. Blakers, *Prog. Photovolt. Res. Appl.* 2013, **21**, 490–499.1.



**TOC:** Robust all inorganic solar cells showing 1.7% efficiency were fabricated entirely from solution in air onto non-conductive glass using solution soluble nanocrystal inks.